9

Optical Holography Reconstruction of Nano-objects

Cesar A. Sciammarella[1,2], Luciano Lamberti[2] and
Federico M. Sciammarella[1]
[1]*College of Engineering & Engineering Technology, Northern Illinois University,*
[2]*Dipartimento di Ingegneria Meccanica e Gestionale, Politecnico di Bari,*
[1]*USA*
[2]*Italy*

1. Introduction

The continuous growth of many fields in nanoscience and nanotecnology puts the demand for observations at the sub-micron level. Electron microscopy and X-rays can provide the necessary short wavelengths to gather information at the nanometer and sub-nanometer range but, in their current form, are not well suited to perform observations in many problems of scientific and technical interest. Furthermore, the environment required for the observation via X-rays or electron microscopy is not suitable for some type of specimens that it is necessary to study. Another concern is the changes that may be induced in the specimen's structure by the utilized radiation. These issues have led to the return to optics and to the analysis of the optical problem of "super-resolution", that is the capacity of producing optical images beyond the classical diffraction limit.

Classical optics has limitations on the resolution that can be achieved utilizing optical microscopy in the observation of events taking place at the sub-micron level, i.e. to a few hundreds of nanometers. To overcome this limitation and achieve super-resolution, non conventional methods of illumination such as evanescent waves are utilized. The initial approach to the utilization of evanescent field properties was the creation of near-field techniques: a probe with dimensions in the nano-range detects the local evanescent field generated in the vicinity of the objects that are observed. A perspective review on super-resolution can be found in Sciammarella (2008).

New methods recently developed by C.A. Sciammarella and his collaborators (see, for example, Sciammarella, 2008; Sciammarella *et al*., 2009) rely on the emission of coherent light by the objects that are under analysis. This is done through the phenomenon of light generation produced by electromagnetic resonance. Object self-luminosity is the consequence of electromagnetic resonance. Why self-luminosity may help to increase resolution? The light generated in this way has particular properties that are not present in the light sent by an object that results from external illumination. The produced wave fronts can travel long distances or go through an optical system without the diffraction changes experienced by ordinary wave fronts (see, for example, Durnin *et al*., 1987; Buchal, 2003; Gutierrez-Vega *et al*., 2001; Hernandez-Aranda *et al*., 2006).

This paper will discuss two alternative approaches to near field techniques: (i) Using diffraction through the equivalent of a diffraction grating to generate an ample spectrum of wave vectors; (ii) Exciting the objects to be observed with the evanescent fields so that the objects become self-luminous. Examples of optical holography reconstruction of nano-objects are presented in the chapter.
The paper is structured as follows. After the Introduction section, evanescent waves and super-resolution are briefly recalled in Section 2. Section 3 describes the experimental setup. Section 4 analyzes the diffraction pattern of a 6 μm diameter polystyrene microsphere immersed in a NaCl solution and illuminated by evanescent light. Section 5 analyzes the system of rectilinear fringes observed in the image. Section 6 describes the process of formation of holograms at the nano-scale. Sections 7 and 8 respectively present the results of optical reconstruction of NaCl nanocrystals and polystyrene nanospheres contained in the saline solution. Finally, Section 9 summarizes the most important findings of this study.

2. Theoretical background

2.1 Properties of evanescent waves

The self generation of light is achieved through the use of total internal reflection (TIR). At the interface between two media such that the index of refraction of medium 1 is larger than the index of refraction of medium 2 (i.e. $n_1>n_2$), if a light beam is incident with an angle $\theta_i>\theta_{i,crit}$, a total reflection of the beam, in which essentially all of the light is reflected back into the first medium, takes place (Fig. 1a). Even though the light no longer propagates into the second medium, there is a small amount of penetration of the electromagnetic field across the interface between the two media. In the vector form solution of Maxwell equations, it can be shown that, under the condition of total reflection, the electromagnetic field does not disappear in the second medium (Born and Wolf, 1999). However, there is no energy exchange with the second medium. The components of the electromagnetic field transmitted in the second medium, vectors **E** and **H**, depend on (Born and Wolf, 1999):

$$\exp\left[-i\frac{2\pi}{\lambda}z\sqrt{\frac{\sin^2\theta_i}{n_{12}^{\ 2}}-1}\right] \tag{1}$$

where the relative index of refraction is defined as $n_{12}=n_2/n_1$.
The intensity of the field decays by 1/ e at the distance z from the interface equal to:

$$z=\frac{\lambda}{2\pi\sqrt{\frac{\sin^2\theta_i}{n_{12}^{\ 2}}-1}} \tag{2}$$

Under this condition a particular type of waves are produced in the interface (Fig. 1a). These waves are called *evanescent waves* and travel at the interface decaying exponentially in the second medium at a depth that is a fraction of the wavelength of the utilized light as shown by Eq. (2). The decay of electromagnetic field is sketched in Fig. 1a.
The electromagnetic field of evanescent waves hence does not propagate light in the second medium. However, if a dielectric medium or a conducting medium comes in contact with the evanescent field, light is emitted by the medium itself. This interaction depends on the properties, size and geometry of the medium. In the case of a dielectric medium, through

Rayleigh molecular scattering, light is emitted in all directions as illustrated in Fig. 1b. The light emission is a function of the electronic configuration of the medium. If the medium is a metal, the Fermi's layer electrons produce resonances called plasmons. The effect is reversible, photons can generate plasmons, and the decaying plasmons generate photons. In the case of very small dielectric objects, the resonance takes place at the level of the bound electrons. The actual dimensions of the object determine the different resonance modes and light at frequencies different from the frequency of illuminating light is generated.

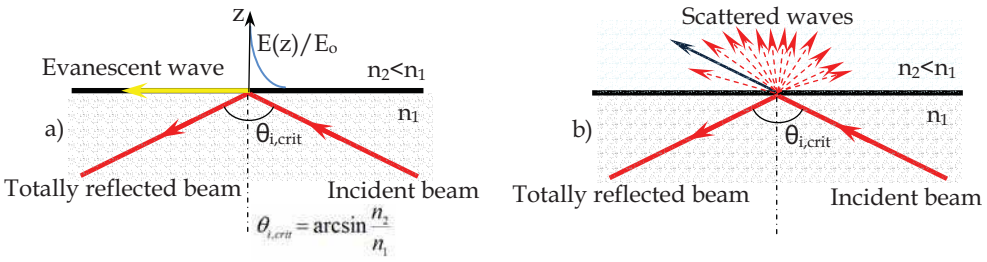

Fig. 1. a) Formation and characteristics of evanescent waves; b) Propagation in a dielectric medium.

According to the Quantum Mechanics principle of preservation of momentum for the photons, some of the energy of the incident beam continues in the second medium (the direction indicated by the blue arrow in Fig. 1b).

2.2 Super-resolution

The possibility of getting higher resolutions depends on the energy available and detector spatial frequency capability. This was foreseen by Toraldo di Francia (Toraldo di Francia, 1952) when he postulated that the resolution of an optical system could be increased almost continuously beyond the classical Rayleigh's diffraction limit, provided that the necessary energy to achieve these results is available. When Toraldo di Francia presented this original work (Toraldo di Francia, 1958) it was argued that his proposed super-resolution approach violated the Heisenberg uncertainty principle. However, the arguments using the Heisenberg principle, those arguments are included in many text books of Optics, can be easily dismissed because they are based on the wave function of a single photon while one is dealing with the wave function of millions of photons. The question can be summarized according to Yu (2000). If ΔE is the amount of energy invested in an observation and Δx is a distance to be measured, the Heisenberg principle can be stated as follows:

$$\Delta E \Delta x \geq \frac{hc}{2} \tag{3}$$

where h is the Planck's constant, c is the speed of light. By increasing the energy there is no limit to the smallness of distance that can be measured. Therefore, increases in smallness of the distance that one wants to measure will require enormous increases in the energy that must be invested. This is because in Eq. (3) there is a large factor: the speed of the light c. There is another important application of the Heisenberg principle that is more relevant to the topic of this chapter and was pointed out by Vigoureux (2003). This relationship is:

$$\Delta x \, \Delta k_x > 2\pi \tag{4}$$

The wave propagation vector has two components $\vec{k_x}$ and $\vec{k_y}$. In Eq. (4), $\vec{k_x}$ is the wave vector component in the x-direction. Vigoureux showed that for waves propagating in the vacuum Eq. (4) leads to the Rayleigh limit of λ/ 2. In order to go beyond the λ/ 2 limit, one must have values of $\vec{k_x}$ falling in the field of evanescent waves. Therefore, to capture evanescent waves is an effective approach to getting super-resolution. This conclusion is in agreement with the conjecture made by Toraldo di Francia in 1952.

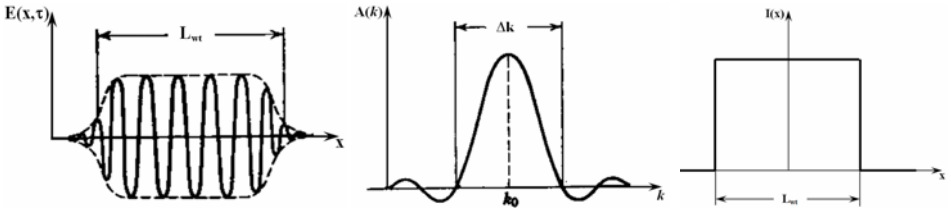

a) b) c)

Fig. 2. a) Harmonic wave train of finite extent L_{wt}; b) Corresponding Fourier spectrum in wave numbers *k*; c) Representation of a spatial pulse of light whose amplitude is described by the rect(x) function.

A further mathematical argument may be based on the Fourier expansion of the Maxwell equation solution. In the classical optics scheme of plane-wave solutions of the Maxwell equations, monochromatic waves of definite frequencies and wave numbers are considered. This idealized condition does not apply in the present case. One can start from the Fourier solution of the Maxwell equations in the vector field (time-space):

$$E(x,\tau) = \frac{1}{\sqrt{2\pi}} \int_{-\infty}^{+\infty} A(k) e^{ikx - i\omega(k)\tau} \, dk \tag{5}$$

where: E(x,τ) is the scalar representation of the propagating electromagnetic field, x is the direction of propagation of the field, τ is the time, A(*k*) is the amplitude of the field, *k* is the wave number 2π/ λ, ω(*k*) is the angular frequency. A(*k*) provides the linear superposition of the different waves that propagate and can be expressed as:

$$\mathrm{A}(k) = \sqrt{2\pi} \;\; \delta(\mathrm{k\text{-}k_o}) \tag{6}$$

where δ(k-k$_o$) is the Dirac's delta function. This amplitude corresponds to a monochromatic wave $E(x,\tau) = e^{ikx - i\omega(k)\tau}$. If one considers a spatial pulse of finite length (Fig. 2a), at the time τ=0, E(ξ,0) is (see Fig. 2c) a finite wave-train of length L_{wt} where A(*k*) is a function spreading a certain length Δk (Fig. 2b). The dimension of L_{wt} depends on the analyzed object size. In the present case, objects are smaller than the wavelength of the light.

Since L_{wt} and Δk are defined as the RMS deviations from the average values of L_{wt} and Δk evaluated in terms of the intensities $|\mathbf{E}(x,0)|^2$ and $|\mathbf{A}(\mathbf{k})|^2$ (Jackson, 2001), it follows:

$$L_{wt} \Delta k \geq \frac{1}{2} \tag{7}$$

Since L_{wt} is very small, the spread of wave numbers of monochromatic waves must be large. Hence there is a quite different scenario with respect to the classical context in which the length L_{wt} is large when compared to the wavelength of light.
In order to simplify the notation, one can reason in one dimension without loss of generality. The spatial pulse of light represented in Fig. 2c is defined as follows:

$$A(x) = A_o rect(x) \tag{8}$$

where: rect(x)=1 for $|x|<1/2$; rect(x)=1/ 2 for $|x|=1/2$; rect(x)=0 elsewhere.
The Fourier transform of the light intensity $[A(x)]^2$ is $[sinc(x)]^2$. To the order 0 it is necessary to add the shifted orders ±1. The function $A(x\pm\Delta x)$ can be represented through the convolution relationship:

$$A(x \pm \Delta x) = \int_{-\infty}^{+\infty} A(x') \cdot \delta(x \pm \Delta x) \cdot dx' \tag{9}$$

where $x'=x\pm\Delta x$. The Fourier transform of the function $A(x\pm\Delta x)$ will be:

$$FT[A(x \pm \Delta x)] = A(f_x) \cdot e^{i[2\pi f_x(\mp \Delta x/ 2)]x} \tag{10}$$

where f_x is the spatial frequency. The real part of Eq. (10) is:

$$\mathrm{Re}\left\{FT[A(x \pm \Delta x]\right\} = A(f_x) \cdot \cos\left\{[2\pi f_x(\mp \Delta x / 2)]x\right\} \tag{11}$$

By taking the Fourier transform of Eq. (11), one can return back to Eq. (9). For the sake of simplicity, the above derivations are in one dimension but can be extended to the 3D case. Brillouin (1930) showed that for a cubic crystal the electromagnetic field can be represented as the summation of plane wave fronts with constant amplitude as assumed in Eq. (5). In such circumstances the above derivation can be extended to 3-D and can be applied to the components of the field in the different coordinates.

3. Experimental setup

Figure 3 shows the schematic representation of the experimental setup. Following the classical arrangement of total internal reflection (TIR), a helium-neon (He-Ne) laser beam with nominal wavelength λ=632.8 nm impinges normally to the face of a prism designed to produce limit angle illumination on the interface between a microscope slide (supported by the prism itself) and a saline solution of sodium-chloride contained in a small cell supported by this slide. Consequently, evanescent light is generated inside the saline solution.
The objects observed with the microscope are supported by the upper face of the microscope slide. Inside the cell filled with the NaCl solution there is a polystyrene microsphere of 6 μm diameter. The microsphere is fixed to the face of the slide through chemical treatment of the contact surface in order to avoid Brownian motions. The polystyrene sphere acts as a relay lens which collects the light wave fronts generated by nano-sized crystals of NaCl resting on the microscope slide. Polystyrene nanospheres also are injected in the solution. More details on the polystyrene sphere and the saline solution are given in the table included in Fig. 3.
The observed image is focused by a microscope with NA=0.95 and registered by a monochromatic CCD attached to the microscope. At a second port, a color camera records color images. The CCD is a square pixel camera with 1600x1152 pixels. The analysis of the

images recorded in the experiment is performed with the Holo Moiré Strain Analyzer software (General Stress Optics, 2008).

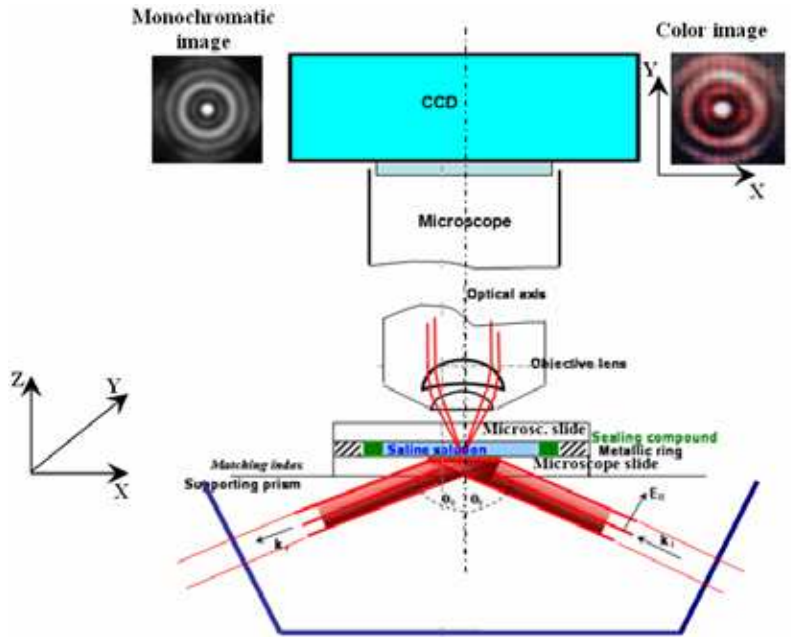

Parameter	Value	Note
Polystyrene microsphere diameter D_{sph}	6 ± 0.042 μm	Tolerance specified by manufacturer
Refraction index of polystyrene sphere n_p	1.57 ± 0.01	Value specified by manufacturer
Refraction index of saline solution n_s	1.36	From NaCl concentration at λ=590 nm

Fig. 3. Experimental set up to image nano-size objects using evanescent illumination. Two CCD cameras are attached to a microscope to record images: monochromatic, color.

Three features can be clearly distinguished in the images recorded by the CCD: the diffraction pattern of the microsphere, a system of rectilinear fringes independent of the microsphere, luminous spots well above the speckle average intensity. These features will be analyzed in detail in the chapter explaining how to extract information from the image.

4. Diffraction pattern of the polystyrene microsphere

Figure 4 shows the image of the diffraction pattern of the 6 μm diameter microsphere (Fig. 4a), the FFT of the pattern (Fig. 4b), and an expanded scale of the central part of the FFT pattern (Fig. 4c). Below are the corresponding images (Figs. 4d-f) of the diffraction pattern of a circular aperture of nominal diameter 6 μm (the classical Airy's pattern). Since the two patterns are different, the wave front of light diffracted by the microsphere is not planar. For this reason, the diffraction pattern of the particle has been simulated with an algorithm based on the multi-corona analysis originally developed by Toraldo di Francia (1952 & 1958) and later reprised by Mugnai *et al.* (2001 & 2004).

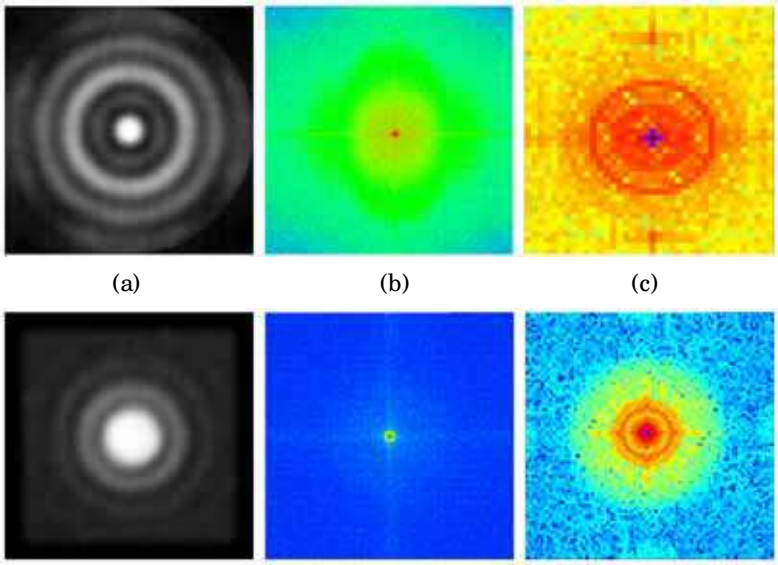

(a) (b) (c)

(d) (e) (f)

Fig. 4. Diffraction pattern of the 6 μm particle and of the 6 μm pinhole: a) Diffraction pattern (6 μm sphere); b) FFT of the diffraction pattern; c) Enlarged view of Fig. 4b); d) Diffraction pattern (6 μm pinhole); e) FFT of the diffraction pattern; f) Enlarged view of Fig. 4e.

In the multi-corona analysis, the 6 μm diameter particle is modeled as a circular pupil of diameter equal to the particle diameter. Let us assume that the pupil of diameter D is divided in N circular coronae by N+1 concentric circumferences. The i^{th} portion of the pupil is thus a circular corona limited by the diameters D_{i-1} and D_i where the generic diameter D_i is defined as $\alpha_i D$. The α_i parameter ranges between 0 and 1 and increases as the corona goes far from the center of the pupil. If all coronae have the same thickness, parameters α_i are in arithmetic progression: 0, 1/ N, 2/ N,…, i/ N,…, 1 (i=1,…,N).

The complex amplitude – expressed as a function of the observation angle θ limited by the position vector of the observation point and the axis perpendicular to the plane of the corona – diffracted by a circular corona limited by D_{int} and D_{ext} is:

$$A(\theta) = \frac{A}{2\lambda \sin\theta}\left[D_{ext} J_1\left(\pi \frac{D_{ext}}{\lambda}\sin\theta\right) - D_{\text{int}} J_1\left(\pi \frac{D_{\text{int}}}{\lambda}\sin\theta\right)\right] \tag{12}$$

where A is the uniform complex amplitude illuminating the corona, λ is the wavelength of the light, and J_1 is the Bessel function of the first order.

Introducing the dimensionless variable $X=\pi D\sin\theta/\lambda$ and summing over the complex amplitudes diffracted by each corona, the total complex amplitude diffracted by the complete pupil comprised of N circular coronae can be expressed as:

$$A(x) = \sum_{i=0}^{N-1} \frac{k_{i+1}}{x}\left[\alpha_{i+1} J_1(\alpha_{i+1} x) - \alpha_i J_1(\alpha_i x)\right] \tag{13}$$

The k_i coefficients were determined by minimizing the difference between the normalized intensity distribution of the diffraction pattern recorded experimentally and its counterpart predicted by the theoretical model (13). For that purpose, the SQP-MATLAB® optimization routine (The MathWorks, 2006) was utilized. Figure 5 compares the experimental results with the predictions of the multi-corona analysis that was extended up to 7 coronae in order to verify the consistency of the algorithm with the experimental data outside of the central region of the pattern. In the central region of the pattern taking three coronae is enough to get an excellent agreement. By increasing the number of coronae the Bessel function expansion (13) captures very well the positions of all the minima and maxima of the experimental curve but causes secondary maxima to reduce in magnitude.

The present results were obtained in the range of visible optics and agree well with the experimental results found by Mugnai *et al*. (Mugnai *et al*, 2001 & 2004) in the microwave range; both phenomena are described very well by the three-coronae theoretical model. Experimental data are consistent also with the results of a theoretical study recently carried out by Ayyagari and Nair (Ayyagari and Nair, 2009) on the scattering of *p*-polarized evanescent waves by a dielectric spherical particle.

It can be seen from Fig. 5 that the central spot of the diffraction pattern observed experimentally is almost two times more narrow in size than its counterpart in the classical Airy's pattern: the position of the first minimum of intensity in the experimental pattern is in fact X=2.05 vs. the classical value of X=3.83 for the Airy's pattern. Therefore, the diffraction pattern of the polystyrene microsphere is equivalent to that produced by a super-resolving pupil.

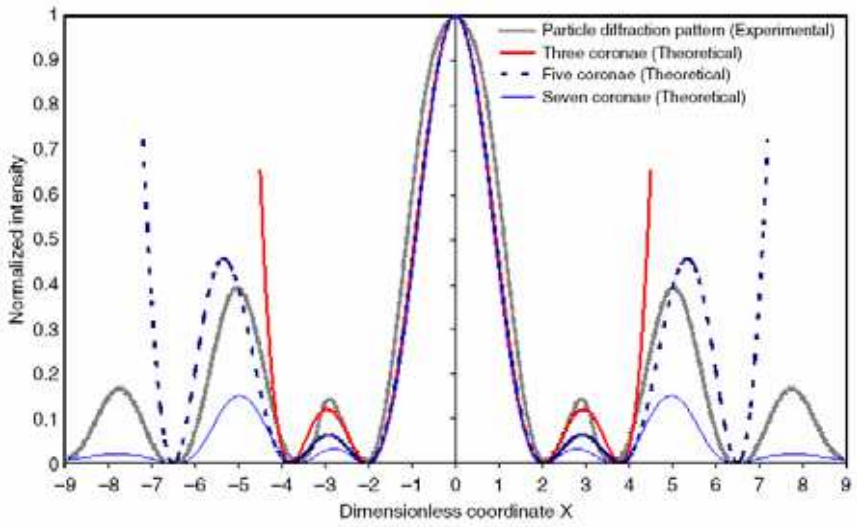

Fig. 5. Comparison between the multi-corona theoretical model and experimental results.

The first step to understand the process of formation of the diffraction pattern observed experimentally is to consider the microsphere as a lens (Fig. 6). The focal distance *f* of this lens can be computed using the equations of geometric optics. The source of the illumination generating the diffraction pattern of the microsphere and the fringes covering the image of

the particle is the resonant electro-magnetic oscillations of interaction of the microsphere with the supporting microscope slide. The whole region of contact between the particle and the microscope slide becomes the equivalent of a micro-laser. The light is generated in the sphere around the first 100 nm in depth and focused in the focal plane of the sphere. The microscope is focused to the plane of best contrast of the diffraction pattern, which must be very close to the microsphere focal plane. The diffraction pattern is not formed by a plane wave front illuminating the microsphere, as is the case with the classical Mie's solution for a diffracting sphere. In the present case, a large number of evanescent wave fronts come in contact with the microsphere and then generate propagating wave fronts that are seen as interference fringes. This mechanism will be clarified in the next section.

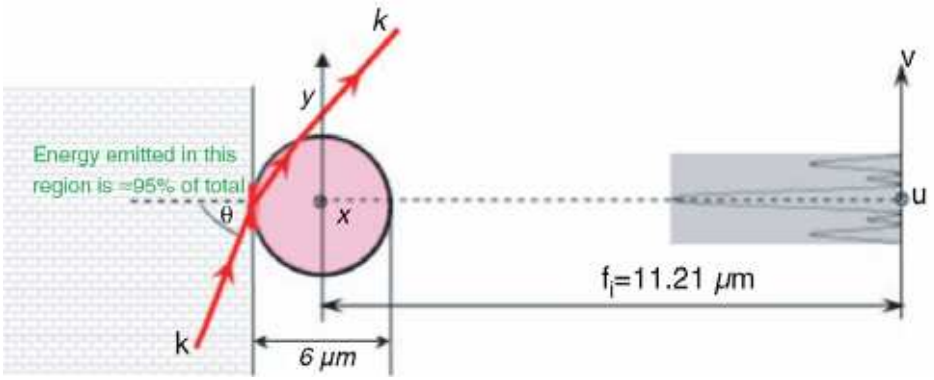

Fig. 6. Polystyrene microsphere modeled as a small spherical lens.

5. System of fringes contained in the recorded image: multi-*k* vector fields

As is mentioned above, besides the diffraction pattern of the polystyrene microsphere, the image recorded by the optical microscope contains also a system of rectilinear fringes. Figure 7 illustrates the process of generation of the evanescent beams that provide the energy required for the formation of the images. The optical setup providing the illumination is similar to the setup originally developed by Toraldo di Francia to prove the existence of evanescent waves (Toraldo di Francia, 1958). A grating is illuminated by a light beam at the limit angle of incidence θ_c. A matching index layer is interposed between the illuminated surface and a prism which is used for observing the propagating beams originated on the prism face by the evanescent waves. In the original experiment conducted by Toraldo di Francia the diffraction orders of the grating produced multiple beams that by interference generated the fringes observed with a telescope. In the present case, the interposed layer corresponds to the microscope slide. Although the microscope slide does not have exactly the same index of refraction of the prism, it is close enough to fulfill its role. The diffraction effect is produced by the residual stresses developed in the outer layers of prism. The multiple illumination beams are the result of residual stresses in the outer layers of the prism. Guillemet (1970) analyzed in detail the process of formation of interference fringes originated by evanescent illumination in presence of residual stresses on glass surfaces. The glass in the neighborhood of surface can be treated as a layered medium and the fringe orders depend on the gradients of index of refraction. A more extensive analysis

of the role played by birefringence in the present example was carried out by Sciammarella and his collaborators (Sciammarella and Lamberti, 2007; Sciammarella *et al.*, 2010).

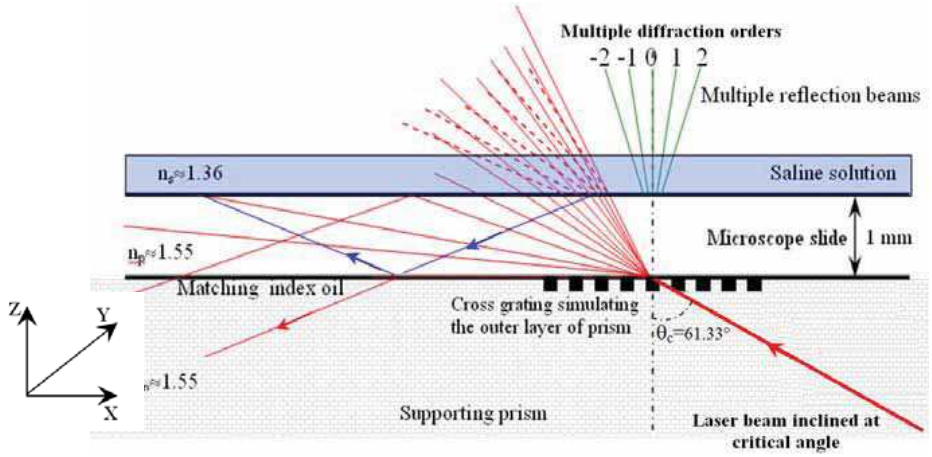

Fig. 7. Model of the interface between the supporting prism and the microscope slide as a diffraction grating causing the impinging laser beam to split into different diffraction orders.

Figure 7 provides a schematic representation of the process of illumination of the observed nano-objects. The laser beam, after entering the prism, impinges on the prism-microscope slide interface, symbolically represented by a grating, where it experiences diffraction. The different diffraction orders enter the microscope slide and continue approximately along the same trajectories determined by the diffraction process. The slight change in trajectory is due to the fact that the indices of refraction of the prism and microscope slide are slightly different. As the different orders reach the interface between the microscope slide and saline solution, total reflection takes place and evanescent wave fronts emerge into the solution in a limited depth that is a function of the wavelength of the light as shown in Eq. (2).

Since the wave fronts are originated by artificial birefringence, for each order of diffraction there are two wave fronts: the *p*-polarized wave front and the *s*-polarized wave front. Upon entering the saline solution these wave fronts originate propagating wave fronts that produce interference fringes. Figure 8 shows the diffraction orders corresponding to one family of fringes extracted from the FT of the image captured by the optical system and contains the diffraction pattern of the microsphere that acts as a relay lens. Since these wave fronts come from the evanescent wave fronts, their sine is a complex number taking values greater than 1. Figure 8 includes also the image extracted from the FT of the central region of the diffraction pattern of the microsphere (the first dark fringe of the microsphere diffraction pattern is shown in the figure) and shows the presence of the families of fringes mentioned above. The fringes form moiré patterns that are modulated in amplitude in correspondence of the loci of the interference fringes of the microsphere. A total of 120 orders can be detected for this particular family (Sciammarella *et al.*, 2010). These wave fronts play a role in the observation of the NaCl nanocrystals contained in the saline solution.

The detail view of Fig. 9 shows the ordinary beam and the extraordinary beam originated by the artificial birefringence of the prism outer layers: birefringence is caused by residual stresses at the boundary between glass slide and prism. The angles of inclination of the

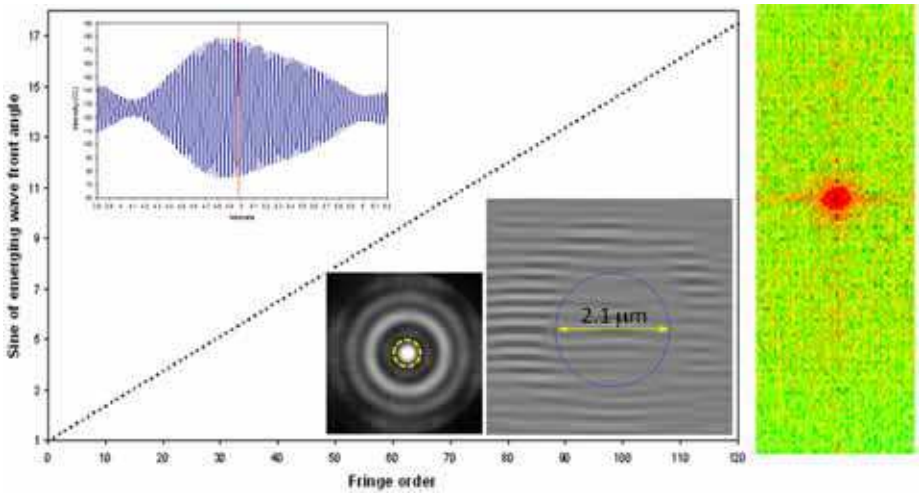

Fig. 8. System of fringes observed in the image of the 6 µm diameter polystyrene sphere. The dotted circle represents the first dark ring in the particle diffraction pattern

ordinary and the extraordinary beams with respect to the normal to the glass slide surface are respectively ϕ_{pp} and ϕ_{sp} where the first subscript "p" and "s" indicates the type of polarization while the second subscript "p" indicates that these wave fronts come from the prism. The *p*-wave front order emerges at the angle ϕ_{pm} in the saline solution while the *s*-wave front emerges at the angle ϕ_{sm} in the saline solution. Those angles can be determined experimentally by utilizing the following relationships:

$$\begin{cases} \sin\phi_{pm}^{\ sper} = \dfrac{\lambda}{p_{pm}} \\ \sin\phi_{sm}^{\ sper} = \dfrac{\lambda}{p_{sm}} \end{cases} \tag{14}$$

where p_{pm} and p_{sm}, respectively, correspond to the spatial frequencies of the two families of fringes formed by the *p* and *s*-waves traveling through the thickness of the glass slide. The pitches p_{pm} and p_{sm} can be measured experimentally by retrieving the sequence of orders produced by the two beams from the FT of the formed images. Since the fundamental pitches of *p* and *s*-wave fringes are, respectively, p_{pm}=3.356 µm and p_{sm}=2.258 µm, the corresponding angles are $\phi_{pm,sper}$=10.860° and $\phi_{sm,sper}$=16.425°.

If the birefringence effect is neglected in the glass slide, the theoretical values of the angles of the *p* and *s*-wave fronts emerging in the saline solution can be expressed as follows (the full derivation is given in Sciammarella *et al.*, 2010):

$$\begin{cases} \sin\phi_{pm} = \dfrac{\sqrt{n_{pp}^{\ 2} - n_g^{\ 2}}}{n_{sol}} \\ \sin\phi_{sm} = \dfrac{\sqrt{n_{sp}^{\ 2} - n_g^{\ 2}}}{n_{sol}} \end{cases} \tag{15}$$

where n_{pp} and n_{sp} are the indices of refraction of the *p* and *s*-waves traveling in the prism; n_g is the refraction index in the glass slide; n_{sol} is the refraction index of the saline solution.
Theoretical values provided by Eq. (15) can be compared with the corresponding values measured experimentally. However, there are two unknowns in Eq. (15): the indices of refraction n_{pp} and n_{sp}. The index of refraction of the glass slide n_g is provided by the manufacturer: 1.5234. The index of refraction of the saline solution can be determined from the solution concentration: 1.36.
The Maxwell-Neumann equations written for the *p* and *s*-wave fronts traveling through the stressed region of the prism are:

$$n_{pp} - n_o = A\sigma_1 + B\sigma_2 \tag{16}$$

$$n_{sp} - n_o = B\sigma_1 + A\sigma_2 \tag{17}$$

where n_o is the index of refraction of the prism in the unstressed state while n_{pp} and n_{sp} correspond to the indices of refraction of the extraordinary wave fronts in the stressed prism. Equations (16) and (17) contain also the constants A and B and the residual compressive stresses σ_1 and σ_2 generated in the prism by the manufacturing process.
By comparing the expressions of the index of refraction n_o of the ordinary beam it follows:

$$n_o = n_{pp} - (A\sigma_1 + B\sigma_2) \;\Leftrightarrow\; n_o = n_{sp} - (B\sigma_1 + A\sigma_2) \tag{18}$$

where the two members of equation (18) must coincide.

$$\begin{cases} Min\left[\Psi(n_{pp}, n_{sp}, A, B, \sigma_1, \sigma_2) = \sqrt{\frac{1}{2}\left[\left(\frac{\sqrt{n_{pp}^2 - n_g^2}}{n_{sol}} - \sin\phi_{pm}^{sper}}{\sin\phi_{pm}^{sper}}\right)^2 + \left(\frac{\frac{\sqrt{n_{sp}^2 - n_g^2}}{n_{sol}} - \sin\phi_{sm}^{sper}}{\sin\phi_{sm}^{sper}}\right)^2\right]}\right] \\ 0.98 \le \left|\frac{n_{pp} - (A\sigma_1 + B\sigma_2)}{n_{sp} - (B\sigma_1 + A\sigma_2)}\right| \le 1.02 \\ 1.5235 \le n_{pp} \le 1.575 \\ 1.5235 \le n_{sp} \le 1.575 \\ -0.8 \cdot 10^{-11} \le A \le -0.3 \cdot 10^{-11} \\ -3.5 \cdot 10^{-11} \le B \le -2.5 \cdot 10^{-11} \\ -180 \cdot 10^6 \le \sigma_1 \le -120 \cdot 10^6 \\ -180 \cdot 10^6 \le \sigma_2 \le -120 \cdot 10^6 \end{cases} \tag{19}$$

The optimization problem (19) was formulated where the objective function Ψ represents the average difference between the theoretical angles at which the *p* and *s*-wave fronts emerge in the saline solution and their counterpart measured experimentally. The Maxwell-Neumann equations were included as constraints in the optimization process: the equality constraint on the ordinary wave, Eq. (18), must be satisfied within 2% tolerance. There are six optimization variables: the two indices of refraction n_{pp} and n_{sp} in the error functional; the two constants *A* and *B* and the residual stresses σ_1 and σ_2 in the constraint equation. The last unknown of the optimization problem, the refraction index n_o corresponding to the unstressed prism, can be removed from the vector of design variables by combing the Maxwell-Neumann relationships into the constraint equation (18).

Three different optimization runs were carried out starting from: (i) lower bounds of design variables (Run A); (ii) mean values of design variables (Run B); (iii) upper bounds of design variables (Run C). The optimization problem (19) was solved by combining response surface approximation and line search (Vanderplaats, 2001). SQP-MATLAB performed poorly as design variables range over very different scales.

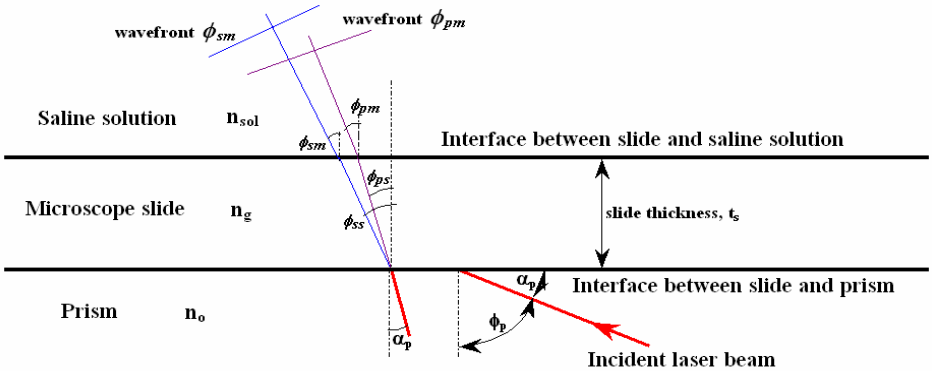

Fig. 9. Schematic of the optical path of *p* and *s*-polarized beams generated by the artificial birefringence of prism.

Parameters	Run A	Run B	Run C
n_{pp}	1.5447	1.5447	1.5468
n_{sp}	1.5716	1.5709	1.5699
n_o	1.5399	1.5399	1.5405
A (m^2/ N)	$-0.5167 \cdot 10^{-11}$	$-0.3017 \cdot 10^{-11}$	$-0.6994 \cdot 10^{-11}$
B (m^2/ N)	$-2.8096 \cdot 10^{-11}$	$-2.9645 \cdot 10^{-11}$	$-3.1390 \cdot 10^{-11}$
C=A–B (m^2/ N)	$2.2929 \cdot 10^{-11}$	$2.6628 \cdot 10^{-11}$	$2.4396 \cdot 10^{-11}$
σ_1 (MPa)	–135.30	–142.50	–161.85
σ_2 (MPa)	–145.01	–145.83	–164.90
τ (MPa)	4.8549	1.6657	1.5279
Residual error Ψ (%)	0.3872	0.2732	0.3394
Error on n_o (%)	1.730	1.673	1.485

Table 1. Results of optimization runs to analyze the effect of artificial birefringence of prism

Optimization results are listed in Table 1. Besides the residual error on the optimized value of Ψ and the constraint margin (18), the table shows also the resulting value of the index of refraction of the ordinary beam n_o, the photoelastic constant $C=A-B$ and the shear stress τ in the prism determined as $|(\sigma_1-\sigma_2)/2|$. Remarkably, the residual error on emerging wave angles is always smaller than 0.39%. The error on refraction index of the ordinary beam is less than 1.75%. The optimization process was completed within 20 iterations.

6. Formation of the holograms at the nano-scale

The wave fronts emerging from the microscope slide play a role in the observation of the prismatic NaCl nanocrystals contained in the saline solution. The observed images are not images in the classical sense but they are lens holograms (theory of Fourier holography is explained in the classical textbook written by Stroke (Stroke, 1969)) generated by the self-luminous nanocrystals. Figure 10 shows the schematic representation of the optical circuit bringing the images to the CCD detector. It can be seen that different diffraction orders emerge from the interfaces of the crystals and the supporting microscope slide. These emerging wave fronts act as multiplexers creating successive shifted images of the object. Let us assume to look at a prism (Fig. 10, Part 1) approximately parallel to the image plane of the CCD. Successive shifted luminous images of the prism are then recorded.

The largest fraction of energy is concentrated in the zero order and the first order (Sciammarella *et al.*, 2009). These orders overlap in an area that depends on the process of formation of the image (see Fig. 10). The order 0 produces an image on the image plane of the optical system, that is centered at a value x of the horizontal coordinate. Let us call S(x) this image. The order +1 will create a shifted image of the particle, S(x-Δx). The shift implies a change of the optical path between corresponding points of the surface. In the present case, the trajectories of the beams inside the prismatic crystals are straight lines and the resulting phase changes are proportional to the observed image shifts. The phase change is:

$$\Delta\phi(x,\Delta x) = K_p\left[S(x) - S(x-\Delta x)\right] \tag{20}$$

where K_p is a coefficient of proportionality. Equation (20) corresponds to a shift of the image of the amount Δx. If the FT of the image is computed numerically, one can apply the shift theorem of the Fourier transform. For a function f(x) shifted by the amount Δx, the Fourier spectrum remains the same but the linear term $\omega_{sp}\Delta x$ is added to the phase: ω_{sp} is the angular frequency of the FT. It is necessary to evaluate this phase change. The shift can be measured on the image by determining the number of pixels representing the displacement between corresponding points of the image (see Fig. 10, Part 4). Through this analysis and using the Fourier Transform it is possible to compute the thickness t of the prism in an alternative way to the procedure that will be described in the following. These developments are a verification of the mechanism of the formation of the images as well as of the methods to determine prism thickness (Sciammarella *et al.*, 2009).

Let us now consider the quasi-monochromatic coherent wave emitted by a nano-sized prismatic crystal. The actual formation of the image is similar to a typical lens hologram of a phase object illuminated by a phase grating (Tanner, 1974). The Fourier Transform of the image of the nanocrystal extended to the complex plane is an analytical function. If the FT is known in a region, then, by analytic continuation, $F(\omega_{sp})$ can be extended to the entire domain. The resolution obtained in this process is determined by the frequency ω_{sp} captured

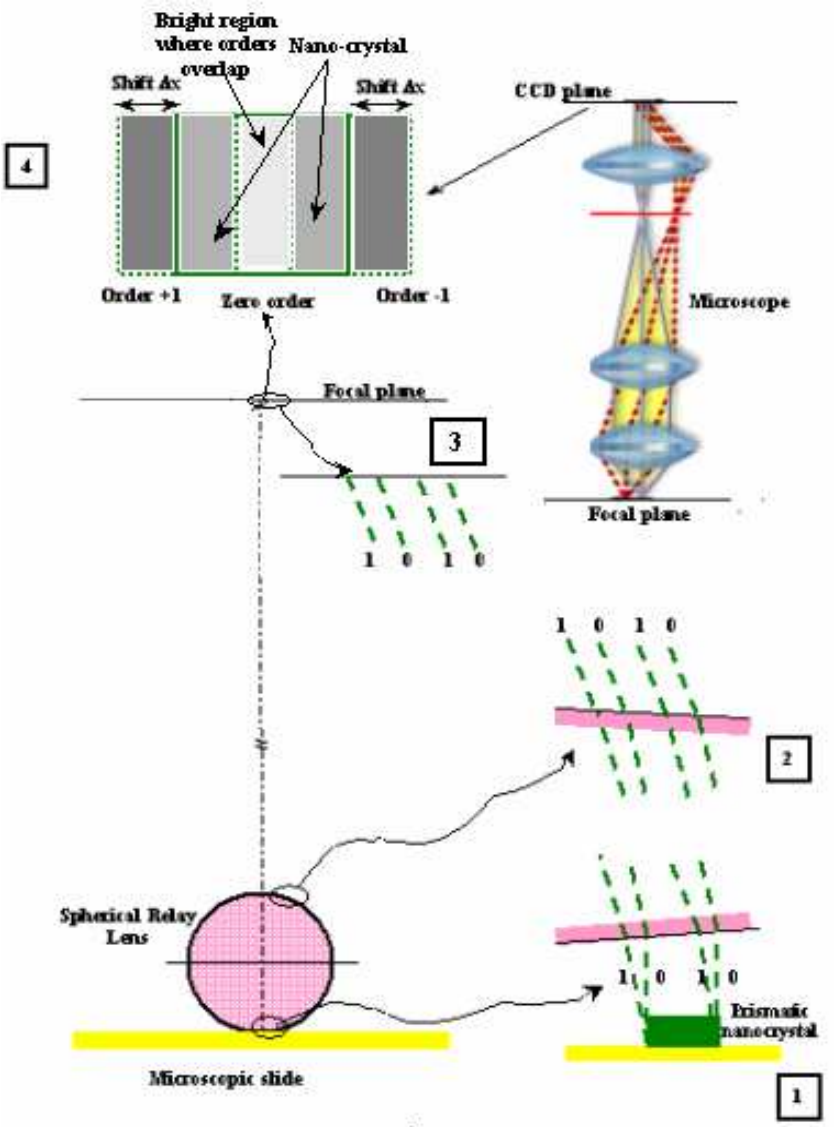

Fig. 10. Schematic representation of the optical system leading to the formation of lens hologram: 1) Prismatic nanocrystal; 2) Wave fronts entering and emerging from the polystyrene micro-sphere acting as a relay lens; 3) Wave fronts arriving at the focal plane of the spherical lens; 4) Wave fronts arriving at the image plane of the CCD. The simulation of the overlapping of orders 0, +1 and -1 in the image plane of the CCD is also shown.

in the image. The image can be reconstructed by a combination of phase retrieval and suitable algorithms. The image can be reconstructed from a $F(\omega_{sp})$ such that $\omega_{sp}<\omega_{sp,max}$, where $\omega_{sp,max}$ is determined by the wave fronts captured by the sensor.

The fringes generated by different diffraction orders experience phase changes that provide depth information. These fringes are carrier fringes that can be utilized to extract optical path changes. This type of setup to observe phase objects was used in phase hologram interferometry as a variant of the original setup proposed by Burch and Gates(Burch et al., 1966; Spencer and Anthony, 1968). When the index of refraction in the medium is constant, the rays going through the object are straight lines. If a prismatic object is illuminated with a beam normal to its surface, the optical path s_{op} through the object is given by the integral:

$$s_{op}(x,y) = \int n_i(x,y,z)dz \tag{21}$$

where the direction of propagation of the illuminating beam is the z-coordinate and the analyzed plane wave front is the plane x-y; $n_i(x,y,z)$ is the index of refraction of the object through which light propagates.
The change experienced by the optical path is:

$$\Delta s_{op}(x,y) = \int_0^t \left[n_i(x,y,z) - n_o \right] dz \tag{22}$$

where t is the thickness of the medium. By assuming that $n_i(x,y,z)=n_c$ where n_c is the index of refraction of the observed nanocrystals, Eq. (22) then becomes:

$$\Delta s_{op}(x,y) = (n_c - n_o)t \tag{23}$$

By transforming Eq. (23) into phase differences and making $n_o=n_s$, where n_s is the index of refraction of the saline solution containing the nanocrystals, one can write:

$$\Delta\phi = \frac{2\pi}{p}(n_c - n_s)t \tag{24}$$

where p is the pitch of the fringes present in the image and modulated by the thickness t of the specimen. In general, the change of optical path is small and no fringes can be observed. In order to solve this problem, carrier fringes can be added. An alternative procedure is the introduction of a grating in the illumination path (Tanner, 1974). In the present case of the nanocrystals, carrier fringes can be obtained from the FT of the lens hologram of analyzed crystals. In the holography of transparent objects, one can start with recording an image without the transparent object of interest. In a second stage, one can add the object and then superimpose both holograms in order to detect the phase changes introduced by the object of interest. In the present experiment, reference fringes can be obtained from the background field away from the observed objects. This procedure presupposes that the systems of carrier fringes are present in the field independently of the self-luminous objects. This assumption is verified in the present case since one can observe fringes that are in the background and enter the nanocrystals experiencing a shift.

7. Observation of prismatic sodium-chloride nanocrystals

The prismatic nanocrystals of sodium-chloride grow on the surface of the microscope slide by precipitation from the saline solution. Different isomers of NaCl nanocrystals are formed and they are the object of dimensional analysis. There is a variety of nano-isomers that can form at room temperature (Hudgins *et al.*, 1997). In this study, only three isomers types and four crystals were analyzed out of a much larger population of possible configurations.

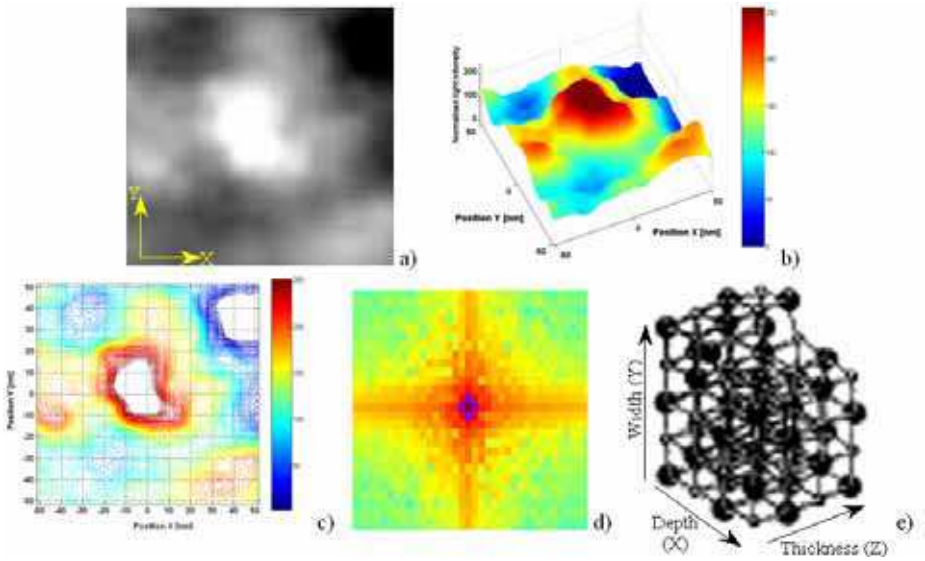

Fig. 11. NaCl nanocrystal of length 54 nm: a) gray-level image (512 x 512 pixels); b) 3-D distribution of light intensity; c) isophote lines; d) FT pattern; e) theoretical crystal structure.

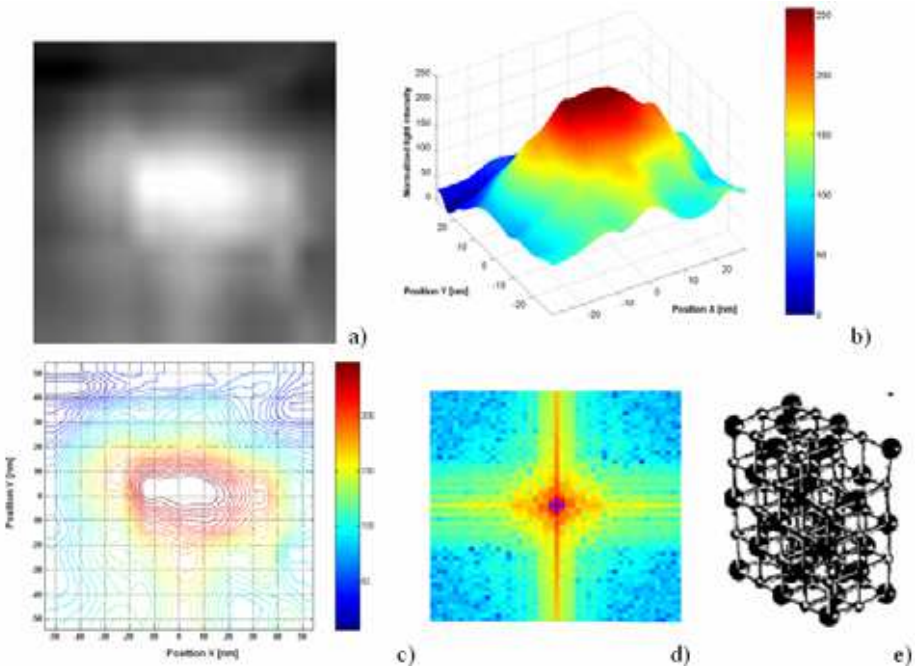

Fig. 12. NaCl nanocrystal of length 55 nm: a) gray level image (512 x 512 pixels); b) 3-D distribution of light intensity; c) isophote lines; d) FT pattern; e) theoretical crystal structure.

The sodium-chloride nanocrystals are located in the recorded images by observing the image of the lens hologram with increasing numerical zooming. A square region around a selected particle is cropped and the image is digitally re-pixelated to either 512×512 pixels or 1024×1024 pixels to increase the numerical accuracy of the FT of the crystals images. Image intensities are also normalized from 0 to 255. Figure 11 shows the nanocrystal referred to as crystal L=54 nm. The isophotes (lines of equal light intensity) of the crystal along with the corresponding isophote level lines and the FT of the image pattern are presented in the figure; the theoretical structure of the nanocrystal is also shown.
A similar representation is given in Fig. 12 for another prismatic crystal with about the same length, that will be referred as crystal L=55 nm.
Figure 13 illustrates the case of a square cross-section crystal that will be called crystal L=86 nm. Figure 13b is an image of the crystal recorded by a color camera; the crystal has a light green tone. The monochromatic image and the color image have different pixel structures, but, by using features of the images clearly identifiable, a correspondence between the images could be established and the image of the nanocrystal located. The picture indicates that the image color is the result of an electromagnetic resonance and not an emission of light at the same wavelength as the impinging light wavelength.

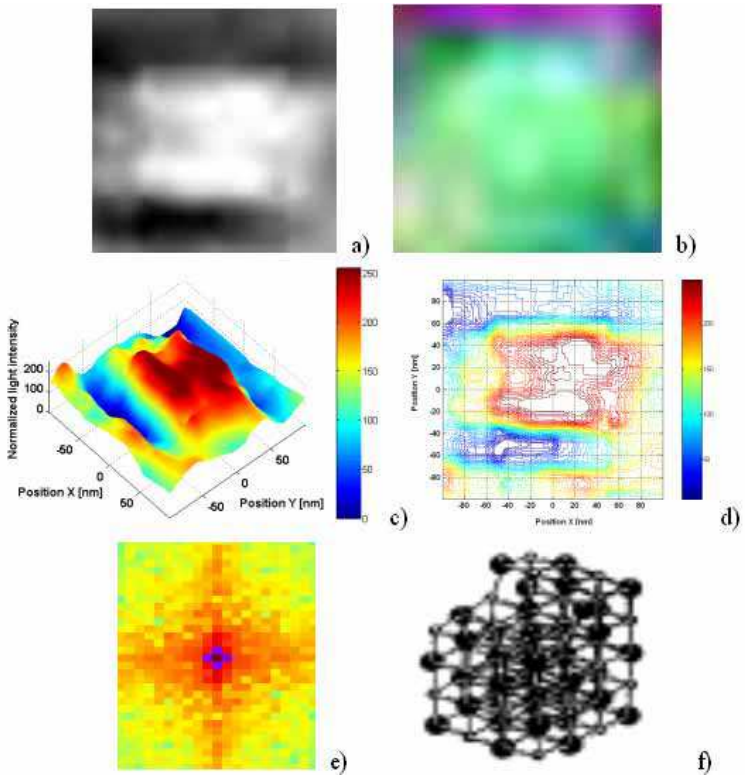

Fig. 13. NaCl nanocrystal of length 86 nm: a) gray-level image (1024 x 1024 pixels); b) image of the crystal captured by a color camera; c) 3-D distribution of light intensity; d) isophote lines; e) FT pattern; f) theoretical crystal structure.

Finally, Fig. 14 is relative to the nanocrystal referred to as crystal L=120 nm.

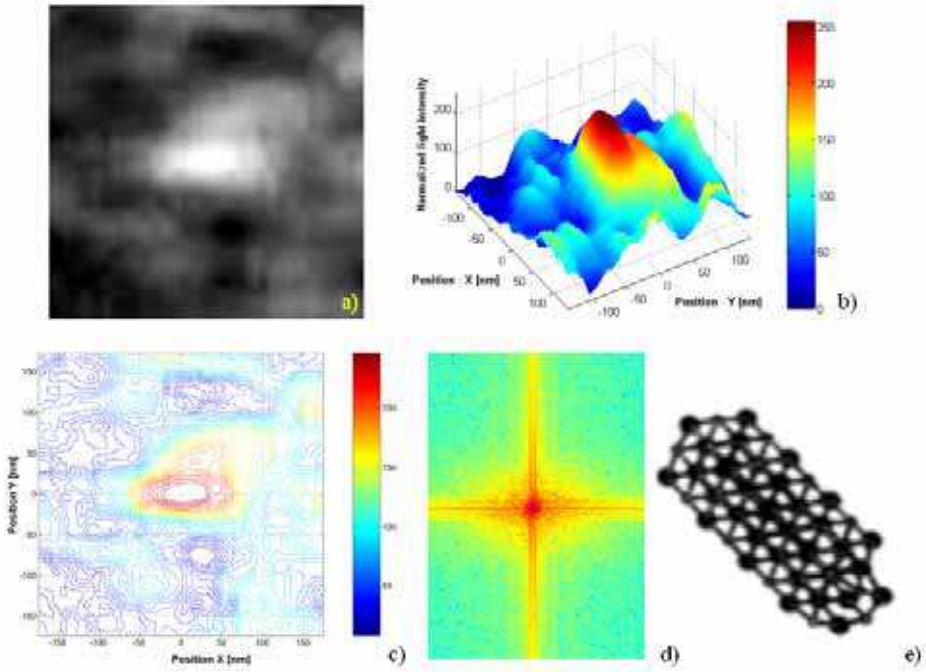

Fig. 14. NaCl nanocrystal of length 120 nm: a) gray-level image (512 x 512 pixels); b) 3-D distribution of light intensity; c) isophote lines; d) FT pattern; e) theoretical crystal structure.

Since the change of phase is very small, fractional orders must be used for measuring the change of optical path as the light travels through nanocrystals. The procedure to obtain depth information from the recorded images is now described. For each analyzed crystal a particular frequency is selected. This frequency must be present in the FT of the image and should be such that the necessary operations for frequency separation are feasible. This means that frequencies that do not depend on the thickness of the nanocrystal must not be near the selected frequency. The frequency of interest is individualized in the background of the observed object. Then, the selected frequency is located in the FT of the object. A proper filter size is then selected to pass a number of harmonics around the chosen frequency. Those additional frequencies carry the information of the change in phase produced by the change of optical path. In the next step, the phase of the modulated carrier and the phase of the unmodulated carrier are computed. The change of phase is introduced in Eq. (24) and the value of t is computed. Since the phase difference is not constant throughout the prismatic crystal face as it is unlikely that the crystal face is parallel to the image plane of camera, an average thickness is computed. The process was repeated for all prismatic crystals analyzed. For the nanocrystal L=86 nm, the face under observation is not a plane but has a step; furthermore, the face is also inclined with respect to the CCD image plane. Hence, depth was computed as an average of the depth coordinates of points of the face.

To completely describe the prisms, one needs to obtain the in-plane dimensions as well. For that purpose, an edge detection technique based on the Sobel filter was utilized in this

study. The edge detection is a difficult procedure since the Goos-Hänchen effect may cause distortions of the wave fronts at the edges. However, a careful procedure allowed the edge detection to be used within a margin of error of a few nanometers. It has to be expected that the prismatic crystals faces are not exactly parallel to the image plane of the camera. Furthermore, due to the integration effect of the pixels on the arriving wave fronts, not all the nanocrystals images can provide meaningful results.

The values of thickness determined for the different nanocrystals were in good agreement with the results provided by the image-shift procedure – Eq. (20) – outlined in Section 6: the standard deviation is within ±5 nm.

Table 2 shows the experimentally measured aspect ratios of nanocrystal dimensions compared with the corresponding theoretical values: the average error on aspect ratios is 4.59% while the corresponding standard deviation is ±6.57%.

Nanocrystal length (nm)	**Experimental dimensions** (nm)	**Experimental aspect ratio**	**Theoretical aspect ratio**
54	72 x 54 x 53	5.43 x 4.08 x 4	5 x 4 x 4
55	55 x 45 x 33.5	4.93 x 4.03 x 3	5 x 5 x 3
86	104 x 86 x 86	4.84 x 4 x 4	5 x 4 x 4
120	120 x 46 x 46	7.83 x 3 x 3	8 x 3 x 3

Table 2. Aspect ratio of the observed nanocrystals: experiments vs. theory

Table 3, on the basis of aspect ratios, shows the theoretical dimensions of the sides of nanocrystals and compares them with the measured values: the average absolute error is 3.06 nm, the mean error is –1.39 nm, the standard deviation of absolute errors is ±3.69 nm. A conservative assumption to estimate the accuracy of measurements is to adopt the smallest dimensions of the crystals as given quantities from which the other dimensions are then estimated. The smallest dimensions are the ones that have the largest absolute errors.

Nanocrystal length (nm)	**Dimensions Measured**	**Dimensions Theoretical**	**Difference** (nm)
	72	66.3	+5.7
54	54	53	+1
	53	53	-----
	55	55.8	-0.8
55	45	55.8	-10.8
	33.5	33.5	-----
	104	107.5	-3.5
86	86	86	0
	86	86	-----
	120	122.7	-2.7
120	46	46	0
	46	46	-----

Table 3. Main dimensions of the observed nanocrystals: experiments vs. theory.

The theoretical structure 5×4×4 corresponding to the crystal L=86 nm has one step in the depth dimension. The numerical reconstruction of this crystal is consistent with the theoretical structure (Fig. 15a); Fig. 15c shows the level lines of the top face; Fig. 15d shows a cross section where each horizontal line corresponds to five elementary cells of NaCl. The crystal shows an inclination with respect to the camera plane that was corrected by means of an infinitesimal rotation. This allowed the actual thickness jump in the upper face of the crystal (see the theoretical structure in Fig. 15b) to be obtained. The jump in thickness is 26 nm out of a side length of 86 nm: this corresponds to a ratio of 0.313 which is very close to theory. In fact, the theoretical structure predicted a vertical jump of one atomic distance vs. three atomic distances in the transverse direction: that is, a ratio of 0.333.

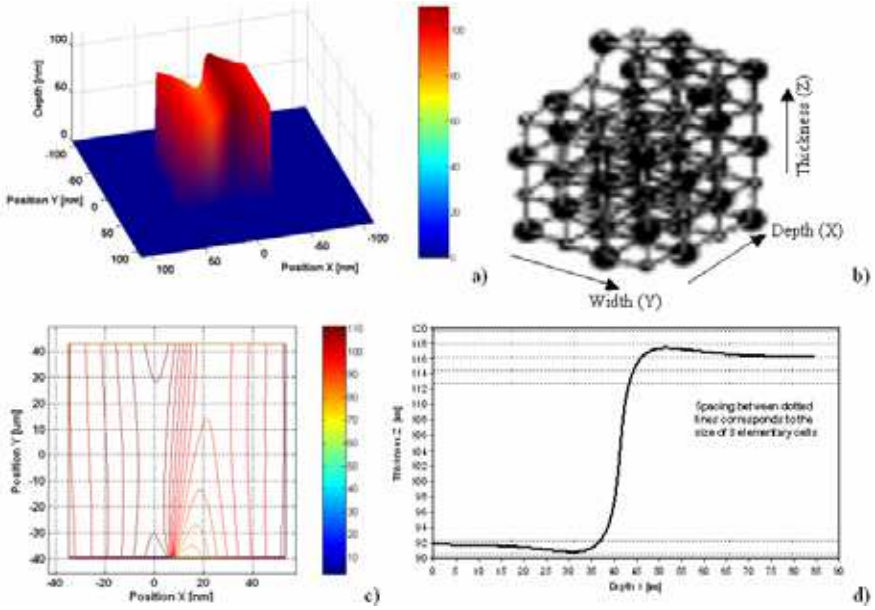

Fig. 15. a) Numerical reconstruction of the NaCl nanocrystal of length 86 nm; b) theoretical structure; c) level lines; d) rotated cross section of the upper face of the nanocrystal: the spacing between dotted lines corresponds to the size of three elementary cells.

8. Observation of the polystyrene nanospheres

Microspheres and nanospheres made of transparent dielectric media are excellent optical resonators. Unlike the NaCl nanocrystals whose resonant modes have not been previously studied in the literature, both theoretical and experimental studies on the resonant modes of microspheres and nanospheres can be found in the literature. Of particular interest are the modes localized at the surface, along a thin equatorial ring. These modes are called *whispering-gallery modes* (WGM). WGM result from light confinement due to total internal reflection inside a high index spherical surface within a lower index medium and from resonance as the light travels a round trip within the cavity with phase matching (Johnson, 1993). The WG modes are within the Mie's family of solutions for resonant modes in light scattering by dielectric spheres. The WG modes can also be derived from Maxwell equations

by imposing adequate boundary conditions (Bohren and Huffman, 1998). They can also be obtained as solutions of the Quantum Mechanics Schrodinger-like equation describing the evolution of a complex angular-momentum of a particle in a potential well.
Figure 16a shows the image of a spherical particle of diameter 150 nm. This image presents the typical WG intensity distribution. Waves are propagating around the diameter in opposite directions thus producing a standing wave with 7 nodes and 6 maxima. The light is trapped inside the particle and there is basically a surface wave that only penetrates a small amount into the radial direction. The signal recorded for this particle is noisier compared with the signal recorded for the prismatic crystals. The noise increase is probably due to the Brownian motion of the spherical particles. While NaCl nanocrystals seem to grow attached to the supporting surface, nanospheres are not in the same condition. Of all resonant geometries a sphere has the capability of storing and confining energy in a small volume.

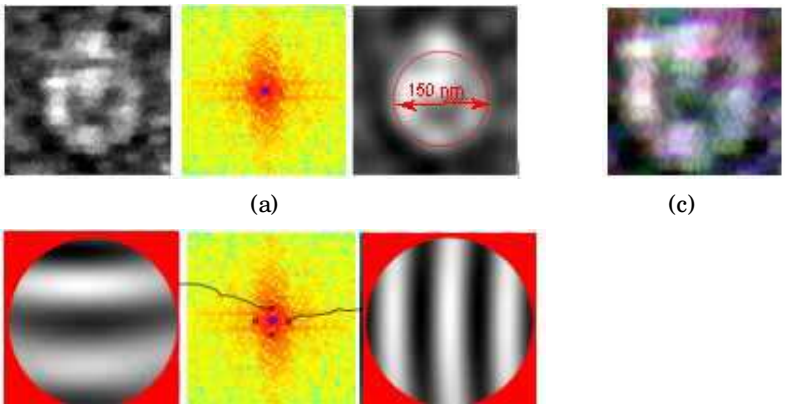

Fig. 16. Spherical nanoparticle of estimated diameter 150 nm: a) FT and zero order filtered pattern; b) systems of fringes modulated by the particle; c) color image of the particle.

The method of depth determination utilized for the nanocrystals can be applied also to the nanospheres. While in prismatic bodies made out of plane surfaces the pattern interpretation is straightforward, in the case of curved surfaces the analysis of the patterns is more complex since light beams experience changes in trajectories determined by the laws of refraction. In the case of a sphere the analysis of the patterns can be performed in a way similar to what is done in the analysis of the Ronchi test for lens aberrations. Figure 16 shows the distortion of a grating of pitch p=83.4 nm as it goes through the nanosphere. The appearance of the observed fringes is similar to that observed in a Ronchi test. The detailed description of this process is not included in this chapter for the sake of brevity.
Figure 17a shows a spherical particle of estimated diameter 187 nm while Fig. 17b shows the average intensity. Figure 17c is taken from Pack (2001) and shows the numerical solution for the WGM of a polystyrene sphere of diameter 1.4 μm while Fig. 17d shows the average intensity. There is good correspondence between experimental results and numerical simulation. The electromagnetic resonance occurs at the wavelength λ=386 nm which corresponds to UV radiation. The color camera is sensitive to this frequency and Fig. 16c shows the color picture of the D=150 nm nanosphere: the observed color corresponds approximately to the above mentioned resonance wavelength.

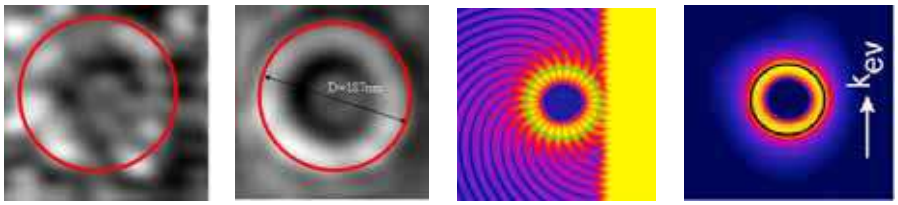

(a) (b) (c) (d)

Fig. 17. Spherical nano-particle of estimated diameter 187 nm: a) Original image; b) Average intensity image; c) Numerical simulation of WG modes; d) Average intensity of numerical simulation.

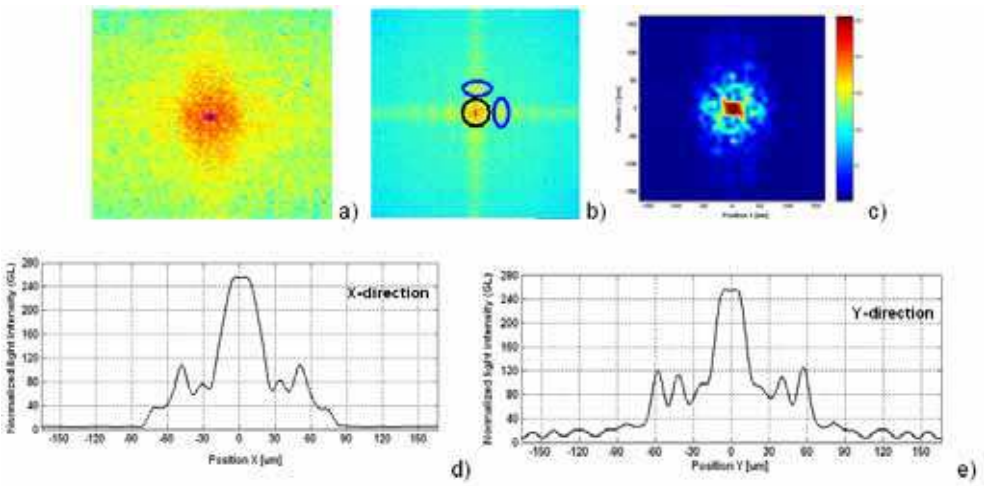

Fig. 18. a) FT pattern of the image of the 150 nm polystyrene nanosphere; b) Fourier transform of the real part of the FT of the nanosphere image; c) 2D view of the zero order extracted from the real part of the FT pattern of the nanosphere image; d) cross-section of the zero order in the X-direction; e) cross-section of the zero order in the Y-direction.

Four particles with radius ranging between 150 and 228 nm were analyzed. For example, Fig. 18 illustrates the different stages involved by the determination of the D=150 nm nanoparticle diameter. The Fourier transform of the image is shown in Fig. 18a while Fig. 18b shows the FT of the real part of the FT of the image. Figure 18c shows the intensity distribution of order 0. Different peaks corresponding to fringe systems present in the image can be observed. Figures 18d-e show the cross sections of the zero order with the corresponding peaks observed in Fig. 18c. These patterns are similar to those observed for the prismatic nanocrystals (Sciammarella *et al.*, 2009). The gray level intensity decays from 255 to 20 within 75 nm: this quantity corresponds to the radius of the nanosphere.

An alternative way to determine diameter from experimental data is based on the WGM properties that relate the diameter or radius of the nanosphere to the standing waves which in turn are characterized by the number of zero nodes or the number of maxima. These numbers depend on the index of refraction and on the radius of the nanosphere. The numerical solution of the WG mode of polystyrene sphere developed by Pack (Pack, 2001)

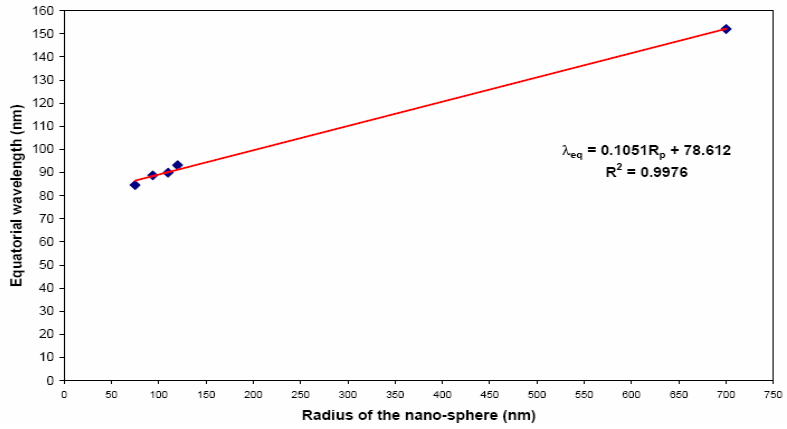

(a)

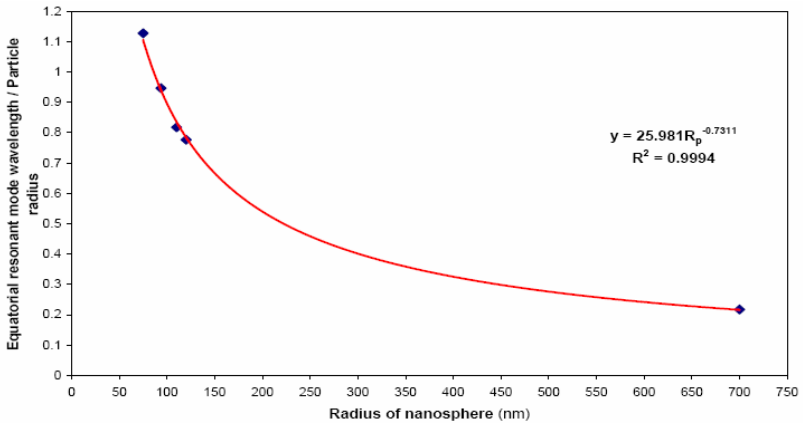

(b)

Fig. 19. Relationships between nanosphere radius and a) equatorial wavelength of the WG mode; b) normalized equatorial wavelength of the WG mode.

was utilized in this study as the resonance modes occur approximately at the same wavelength, λ=386 nm. Figure 19a shows the equatorial wave length of the WG plotted vs. the particle radius. The experimentally measured wavelengths are plotted in a graph that includes also the numerically computed value (radius of 700 nm). A very good correlation (R^2=0.9976) was obtained showing that the edge detection gradient utilized yields values that are consistent with the numerically computed WG wavelengths. The graph shown in Fig. 19b – the ratio of equatorial wavelength to radius is plotted vs. the radius – seems to provide a correlation with a better sensitivity. The correlation was again good (R^2=0.9994).

9. Summary and conclusions

This paper illustrated a new approach to investigations at the nano-scale based on the use of evanescent illumination. The proposed methodology allows to measure topography of

nano-sized simple objects such as prismatic sodium-chloride crystals and spherical polystyrene particles. The basic foundation of the study is that the observed images are lens holographic interferograms of phase objects. The process of formation of those interferograms can be explained in view of the self-luminosity of the observed nano-objects caused by electromagnetic resonance. Another aspect to be considered is the possibility for the generated wave fronts to go through the whole process of image formation without the restrictions imposed by diffraction-limited optical instruments.

Remarkably, nanometer resolution was achieved using an experimental setup including just a conventional optical microscope. Besides the nano-size objects, the diffraction pattern of a 6 μm microsphere illuminated by the evanescent field was also recorded by the sensor. Although the sphere was in the range of the objects that can be visualized by classical microscopy, the diffraction pattern was described by an expansion of the electromagnetic field in a series of Bessel functions and coincided with the typical pattern of a super-resolving pupil. This is again a consequence of electromagnetic resonance phenomena taking place in regions with dimensions smaller than the wavelength of the light.

A great deal of theoretical developments is required to substantiate the experimentally observed properties of the illumination resulting from evanescent waves. However, it can be said that, from the point of view of direct application of these properties, it is possible to access the nano-range utilizing far-field observations. The results presented in the paper indicate that evanescent illumination is the key to making Experimental Mechanics methodologies well suitable for nano-engineering applications.

10. References

Ayyagari, R.S. and Nair, S. (2009). Scattering of P-polarized evanescent waves by a spherical dielectric particle. *Journal of the Optical Society of America, Part B: Optical Physics*, Vol. 26, pp. 2054-2058.

Bohren, C.F. and Huffman, D.R. (1998). *Absorption and Scattering of Light by Small Particles*. Wiley, New York (USA), ISBN: 978-0471293408.

Born, M. and Wolf, E. (1999). *Principles of Optics*. VII Edition. Cambridge University Press, Cambridge (UK), ISBN: 978-0521642224.

Bouchal, Z. (2003). Non diffracting optical beams: physical properties, experiments, and applications. *Czechoslovak Journal of Physics*, Vol. 53, pp. 537-578.

Brillouin, L. (1930). Les électrons dans les métaux et le classement des ondes de de Broglie correspondantes. *Comptes Rendus Hebdomadaires des Séances de l'Académie des Sciences,* Vol. 191, pp. 292-294.

Burch, J.W., Gates, C., Hall, R.G.N. & Tanner, L.H. (1966). Holography with a scatter-plate as a beam splitter and a pulsed ruby laser as light source. *Nature*, Vol. 212, pp. 1347-1348, 1966.

Durnin, J., Miceley, J.J. & Eberli, J.H. (1987). Diffraction free beams. *Physical Review Letters*, Vol. 58, pp. 1499-1501.

General Stress Optics Inc. (2008) *Holo-Moiré Strain Analyzer Version 2.0, Chicago (IL), USA*. http:/ / www.stressoptics.com

Guillemet, C. (1970) *L'interférométrie à ondes multiples appliquée à détermination de la répartition de l'indice de réfraction dans un milieu stratifié*. Ph.D. Dissertation, University of Paris, Paris (France).

Gutiérrez-Vega, J.C., Iturbe-Castillo, M.D., Ramirez, G.A., Tepichin, E., Rodriguez-Dagnino, R.M., Chávez-Cerda, S. & New, G.H.C. (2001). Experimental demonstration of optical Mathieu beams. *Optics Communications*, Vol. 195, pp. 35-40.

Hernandez-Aranda, R.I., Guizar-Sicairos, M. & Bandres, M.A. (2006). Propagation of generalized vector Helmholtz–Gauss beams through paraxial optical systems. *Optics Express*, Vol. 14, pp. 8974–8988.

Hudgins, R.R., Dugourd, P., Tenenbaum, J.N. & Jarrold, M.F. (1997). Structural transitions of sodium nanocrystals. *Physical Review Letters*, Vol. 78, pp. 4213-4216.

Jackson, J.D. (2001). *Classical Electrodynamics*, *Third Edition*. John Wiley & Sons, New York (USA), ISBN: 978-0471309321.

Johnson, B.R. (1993). Theory of morphology-dependent resonances - shape resonances and width formulas. *Journal of the Optical Society of America, Part A: Optics Image Science and Vision*, Vol. 10, pp. 343-352.

Mugnai, D., Ranfagni, A. & Ruggeri, R. (2001). Pupils with super-resolution. *Physics Letters*, Vol. A 311, pp. 77-81.

Mugnai, D., Ranfagni, A. & Ruggeri, R. (2004). Beyond the diffraction limit: Super-resolving pupils. *Journal of Applied Physics*, Vol. 95, pp. 2217-2222.

Pack, A. (2001). *Current Topics in Nano-Optics*. PhD Dissertation. Chemnitz Technical University, Chemnitz (Germany).

Sciammarella, C.A. (2008). Experimental mechanics at the nanometric level. *Strain*, Vol. 44, pp. 3-19.

Sciammarella, C.A. and Lamberti, L. (2007). Observation of fundamental variables of optical techniques in nanometric range. In: *Experimental Analysis of Nano and Engineering Materials and Structures* (E.E. Gdoutos Ed.). Springer, Dordrecht (The Netherlands), ISBN: 978-1402062384.

Sciammarella, C.A., Lamberti, L. & Sciammarella, F.M (2009). The equivalent of Fourier holography at the nanoscale. *Experimental Mechanics* , Vol. 49, pp. 747-773.

Sciammarella, C.A., Lamberti, L. & Sciammarella, F.M. (2010). Light generation at the nano scale, key to interferometry at the nano scale. *Proceedings of 2010 SEM Annual Conference & Exposition on Experimental and Applied Mechanics*. Indianapolis (USA), June 2010.

Spencer, R.C. and Anthony, S.A. (1968). Real time holographic moiré patterns for flow visualization. *Applied Optics*, Vol. 7, p. 561.

Stroke, G.W. (1969). *An Introduction to Coherent Optics and Holography*, *2nd Edition*. Academic Press, New York (USA), ISBN: 978-0126739565.

Tanner, L.H. (1974). The scope and limitations of three-dimensional holography of phase objects. *Journal of Scientific Instruments*, Vol. 7, pp. 774-776.

The MathWorks Inc. *MATLAB® Version 7.0*, Austin (TX), USA, 2006. http:/ / www.mathworks.com

Toraldo di Francia, G. (1952). Super-gain antennas and optical resolving power. *Nuovo Cimento*, Vol. S9, pp. 426-435.

Toraldo di Francia, G. (1958). *La Diffrazione della Luce*. Edizioni Scientifiche Einaudi, Torino (Italy).

Vanderplaats, G.N. (2001). *Numerical Optimization Techniques for Engineering Design*, 3rd Edn. VR&D Inc., Colorado Springs (USA), 2001, ISBN: 978-0944956014.

Vigoureux, J.M. (2003). De l'onde évanescente de Fresnel au champ proche optique. *Annales de la Fondation Luis de Broglie*, Vol. 28, pp. 525-547.

Yu, F.T.S. (2000). *Entropy and Information Optics*. Marcel Dekker, New York (USA), ISBN: 978-0824703639.

Holography, Research and Technologies

Edited by Prof. Joseph Rosen

ISBN 978-953-307-227-2
Hard cover, 454 pages
Publisher InTech
Published online 28, February, 2011
Published in print edition February, 2011

Holography has recently become a field of much interest because of the many new applications implemented by various holographic techniques. This book is a collection of 22 excellent chapters written by various experts, and it covers various aspects of holography. The chapters of the book are organized in six sections, starting with theory, continuing with materials, techniques, applications as well as digital algorithms, and finally ending with non-optical holograms. The book contains recent outputs from researches belonging to different research groups worldwide, providing a rich diversity of approaches to the topic of holography.

How to reference

In order to correctly reference this scholarly work, feel free to copy and paste the following:

Cesar A. Sciammarella, Luciano Lamberti and Federico M. Sciammarella (2011). Optical Holography Reconstruction of Nano-objects, Holography, Research and Technologies, Prof. Joseph Rosen (Ed.), ISBN: 978-953-307-227-2, InTech, Available from: http://www.intechopen.com/books/holography-research-and-technologies/optical-holography-reconstruction-of-nano-objects

INTECH
open science | open minds

InTech Europe
University Campus STeP Ri
Slavka Krautzeka 83/A
51000 Rijeka, Croatia
Phone: +385 (51) 770 447
Fax: +385 (51) 686 166
www.intechopen.com

InTech China
Unit 405, Office Block, Hotel Equatorial Shanghai
No.65, Yan An Road (West), Shanghai, 200040, China
中国上海市延安西路65号上海国际贵都大饭店办公楼405单元
Phone: +86-21-62489820
Fax: +86-21-62489821